



Journal of Geophysical Research: Solid Earth

Supporting Information for

Radially Anisotropic Seismic Structure of the Antarctic Upper Mantle Based on Full-Waveform Adjoint tomography

A. J. Lloyd¹, D. A. Wiens¹, H. Zhu², J. Tromp³, A. A. Nyblade⁴, R. C. Aster⁵, S. E. Hansen⁶, I. W. D. Dalziel⁷, T. J. Wilson⁸, E. R. Ivins⁹, and J. P. O'Donnell

¹Department of Earth & Planetary Sciences, Washington University in St. Louis

²Department of Geosciences, The University of Texas at Dallas

³Department of Geosciences and Program in Applied & Computational Mathematics,
Princeton University

⁴Department of Geosciences, Pennsylvania State University

⁵Department of Geosciences, Colorado State University

⁶Department of Geological Sciences, The University of Alabama

⁷Institute for Geophysics, Jackson School of Geosciences, The University of Texas at
Austin

⁸Byrd Polar Research Center and School of Earth Sciences, The Ohio State University

⁹Jet Propulsion Laboratory, California Institute of Technology

¹⁰School of Earth and Environment, The University of Leeds

Contents of this file

Figures S1 to S7

Additional Supporting Information (Files uploaded separately)

Captions for Tables S1

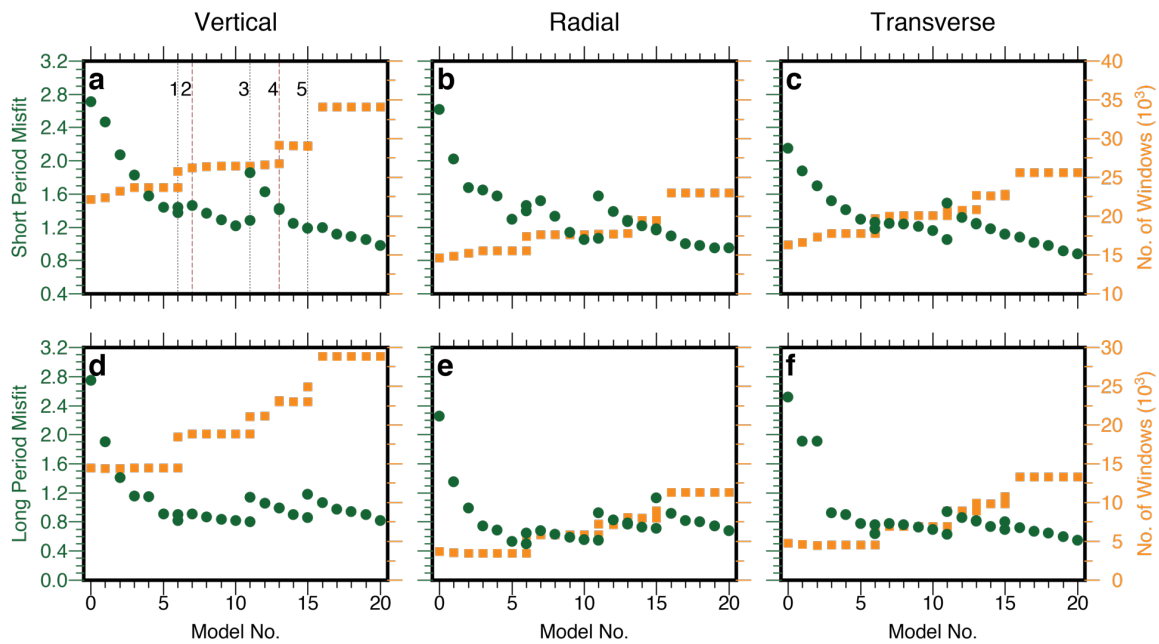


Figure S1. Evolution of the phase misfit (green circles) and the number of measurement windows (orange squares) for each of the six measurement categories. The black dotted lines indicate when the short period corner of the long period band was decreased from (1) 50 s to 40 s, (3) then to 30 s, and (5) finally to 25 s. The red dashed lines indicate (2) when seismic data from international stations located in East Antarctica and (4) when new earthquake waveforms recorded in 2016 were added to the adjoint inversion.

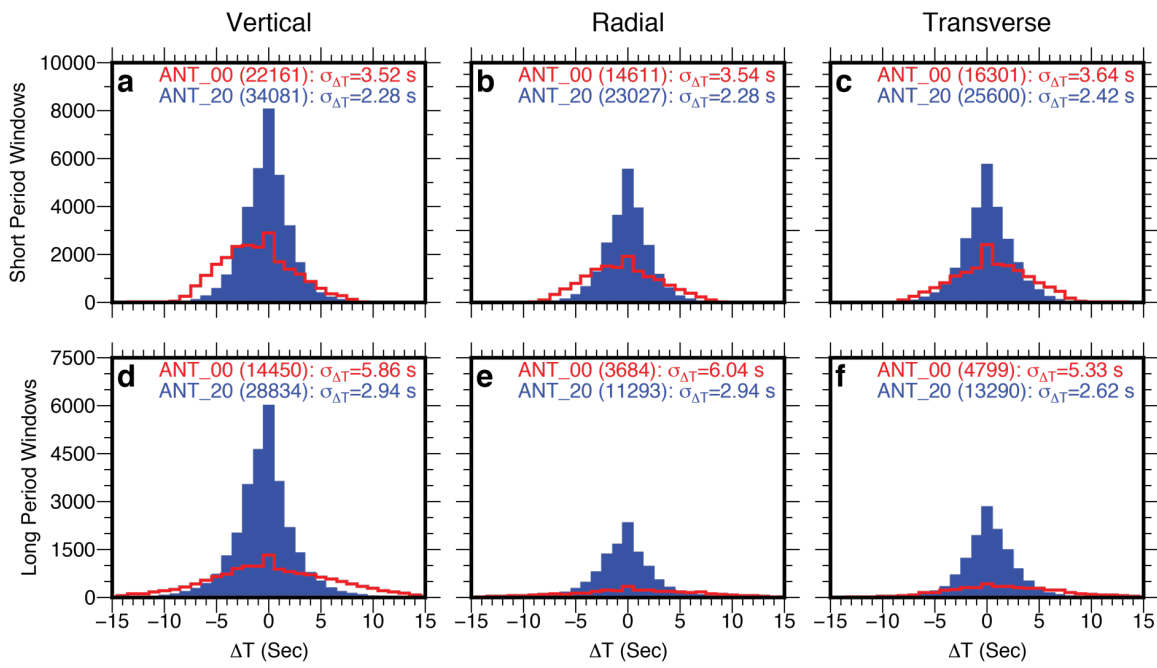


Figure S2. Histograms for each of the six measurement categories showing the travelttime phase difference between the observed and synthetic seismograms for the starting model ANT-00 (red) and the final model ANT-20 (blue).

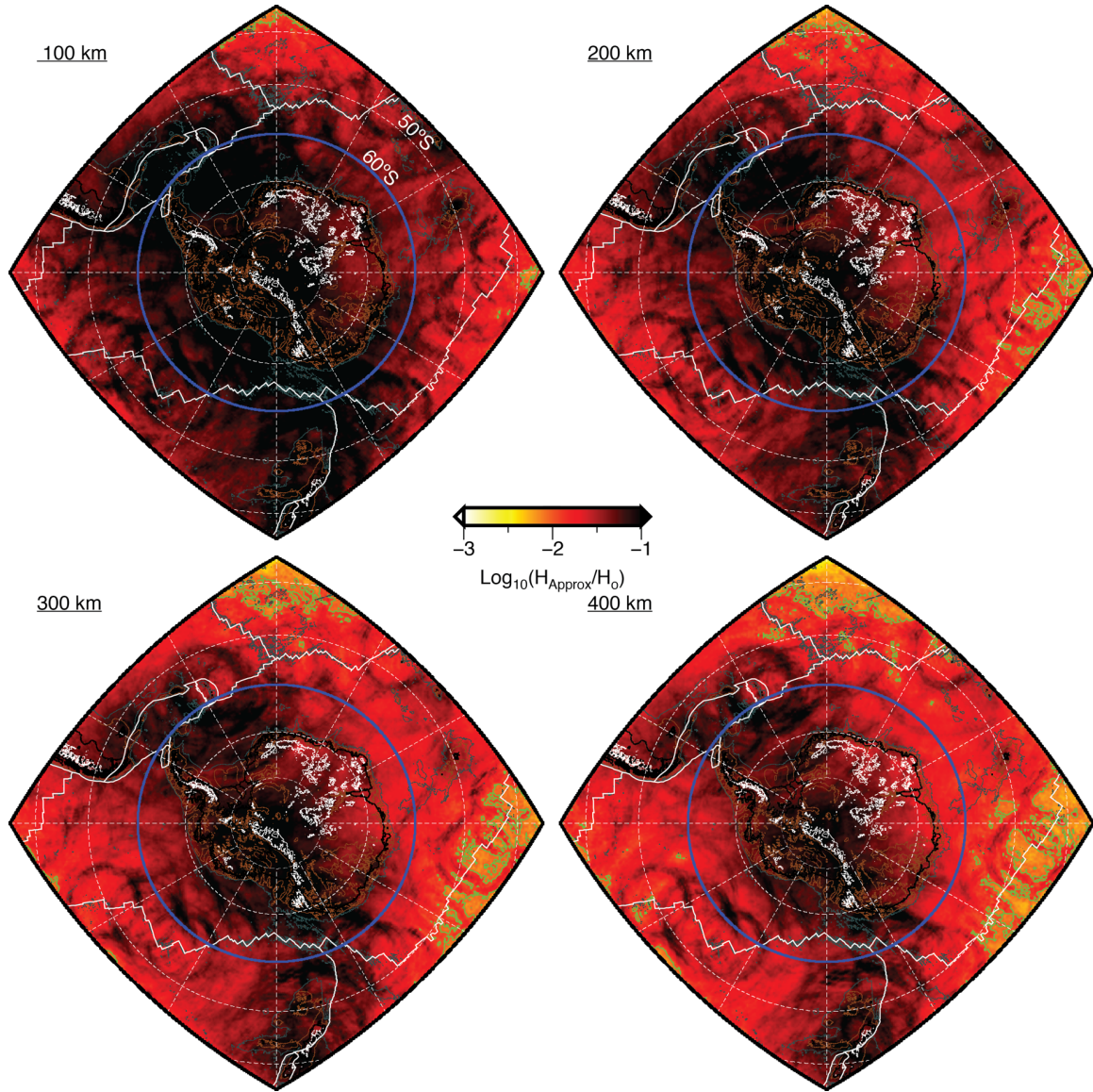


Figure S3. The approximate Hessian (eq. 5) used in the final model update is shown at 100, 200, 300, and 400 km depth, and its variations serve as a proxy for relative data coverage. The thin green line denotes the -2 contour of $\text{Log}_{10}(\text{H}_{\text{approx}}/\text{H}_0)$. A blue line at 60°S denotes the northern boundary of the tomographic images shown in [this study](#). Bathymetry and bedrock topography contours are shown for 1000 m (thin white line) and -500 m (thin brown line), as well as -2500 m (thin dark gray line) elevation in the oceans [[Fretwell et al., 2013](#)]. Thicker white lines denote the plate boundaries [[Bird, 2003](#)], while dashed black lines are lines of latitude every 10° or lines of longitude every 30° .

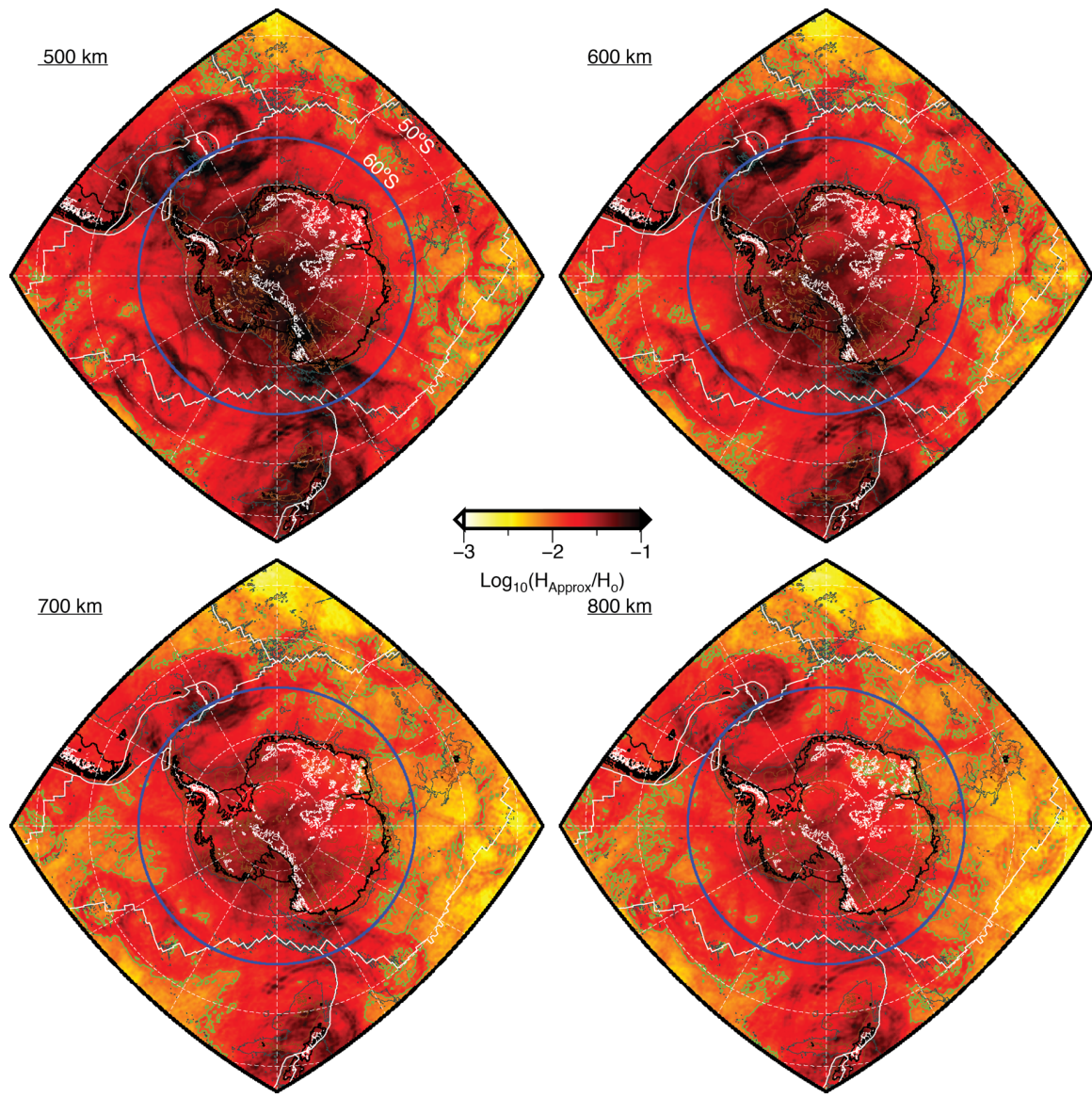


Figure S4. The same as Figure S7 except the approximate Hessian (eq. 5) used in the final model update is shown at 500, 600, 700, and 800 km depth.

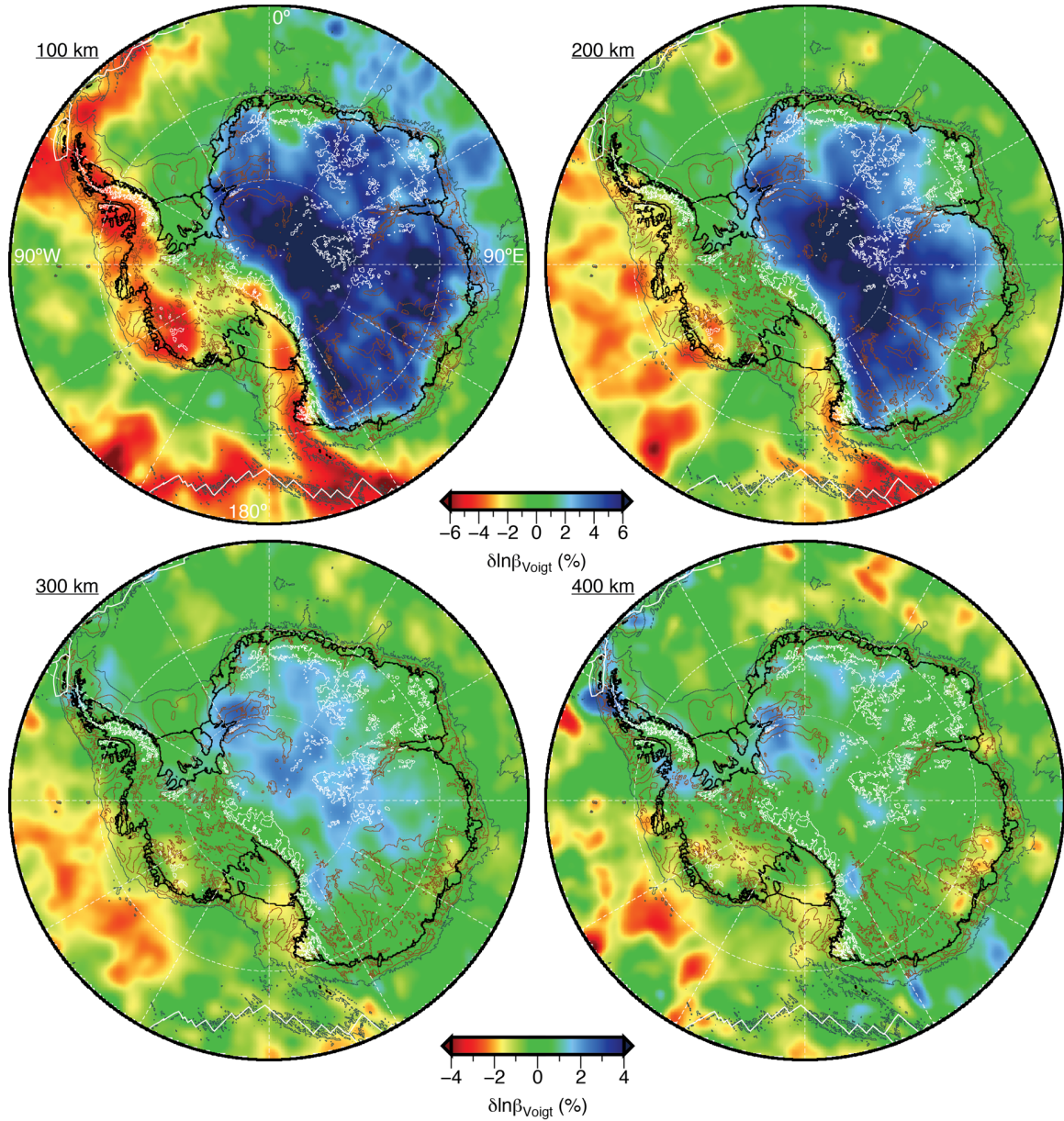


Figure S5. Tomographic images of the Voigt average shear wave speed structure of ANT-20 at 100, 200, 300, and 400 km depth with respect to sea level. Please note at 400 km depth the range of the color scale changes to +/-4%. Mantle velocity anomalies are relative to the 1-D earth model STW105 [Kustowski et al., 2008], which has been slightly modified to account for the topography of 1st and 2nd order seismic discontinuities. Bathymetry and bedrock topography contours are shown for 1000 m (thin white line) and -500 m (thin brown line), as well as -2500 m (thin dark gray line) elevation in the oceans [Fretwell et al., 2013]. Thicker white lines denote the plate boundaries [Bird, 2003], while dashed white lines are lines of latitude every 10° or lines of longitude every 30°.

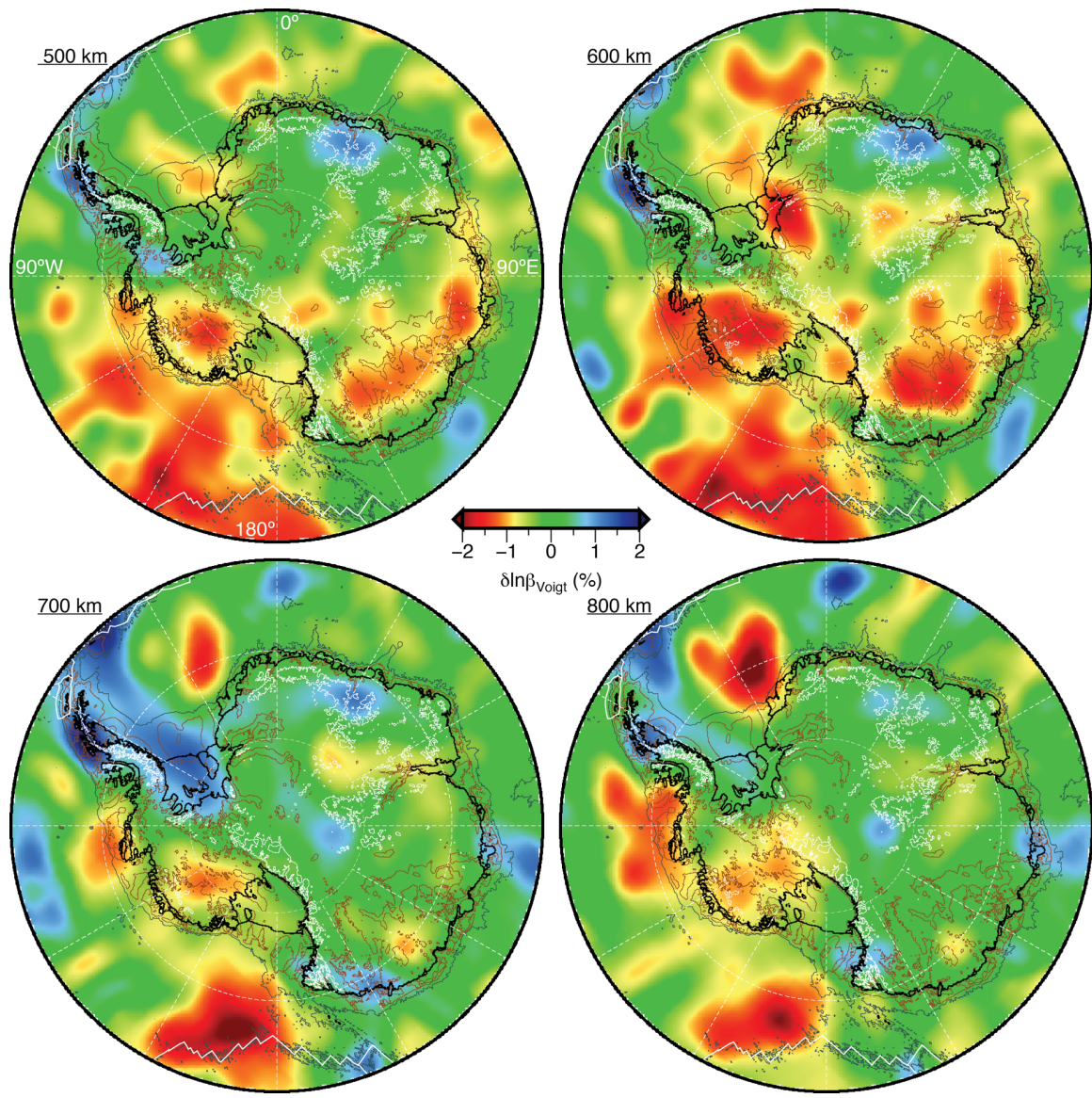


Figure S6. The same as Figure S9 except the Voigt average shear wave speeds of ANT-20 are from 500, 600, 700, and 800 km depth.

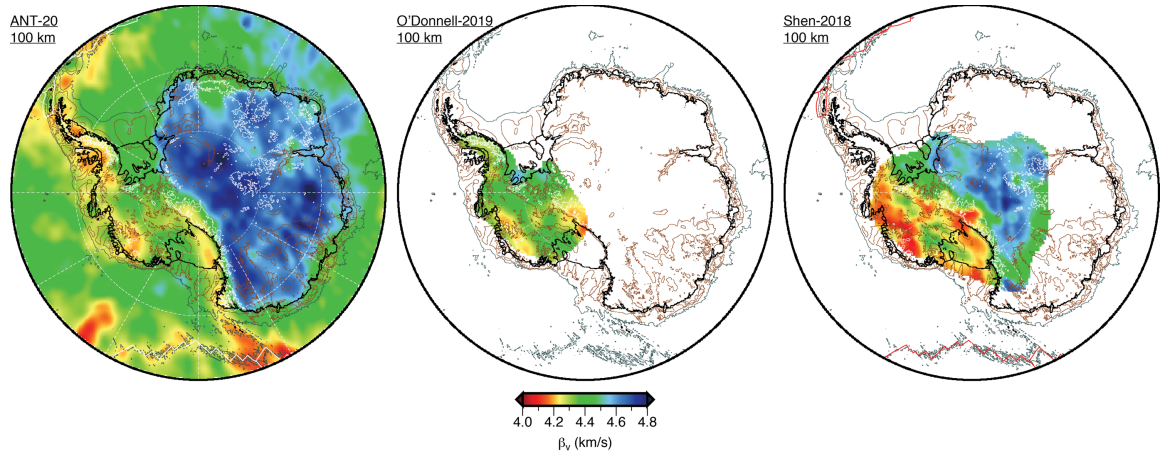


Figure S7. A comparison of the vertically polarized shear-wave speeds at 100 km depth from ANT-20 with those reported by O'Donnell et al. (2019) and Shen et al. (2018a). Note the greater similarities between ANT-20 and O'Donnell et al. (2019) than ANT-20 and Shen et al. (2018a). As discussed in Section 4.3 of the main document, the large difference arises, in part, from the difference in attenuation structure used to account for anelasticity.

Table S1. List of the broadband seismic stations utilized in the adjoint tomographic inversion and their data archive. Please note this table has been uploaded as a separate file (Table_S1.xlsx).